UNIVERSITY OF OKLAHOMA

GRADUATE COLLEGE

ADSORPTION CHARACTERISTICS OF SODIUM DODECYL SULFATE ON ZWITTERIONIC FUNCTIONALIZED ALUMINA: A MOLECULAR DYNAMICS STUDY

A THESIS

SUBMITTED TO THE GRADUATE FACULTY

in partial fulfillment of the requirements for the

Degree of

MASTER OF SCIENCE

By

GARRETT MITCHELL TOW
Norman, Oklahoma
2017

ADSORPTION CHARACTERISTICS OF SODIUM DODECYL SULFATE ON ZWITTERIONIC FUNCTIONALIZED ALUMINA: A MOLECULAR DYNAMICS STUDY

A THESIS APPROVED FOR THE
SCHOOL OF CHEMICAL, BIOLOGICAL AND MATERIALS ENGINEERING

BY

_____
Dr. Liangliang Huang, Chair

_____
Dr. Jeffrey Harwell

_____
Dr. Brian Grady

_____
Dr. Mashhad Fahes

Acknowledgements

I would first and foremost like to acknowledge Dr. Liangliang 'Paul' Huang for his willingness to accept me into his research group during the Junior year of my undergraduate studies. The direction of my life has been massively changed since being introduced to the world of research. Previously without a desire for any particular career path, Paul has been instrumental in guiding me towards a life in research. He has sacrificed a significant amount of his time and energy to ensure that I have been equipped with the knowledge and experiences required to succeed in our research field. Through Paul's efforts, I have attended workshops, conferences, and even had the opportunity to enjoy a summer in China working with collaborators. If anyone in my life has set an example for how I desire to professionally mentor in the future, it has been Paul.

I would like to thank Dr. Chang Liu for his support and hospitality during my stay in Nanjing, China. The opportunity to embrace another culture for a non-trivial span of time has truly impacted my outlook on the world.

Yet another acknowledgement of appreciation is due to Dr. Brian Grady for the discussions we have had, as well as our shared experiences overseas. I am also compelled to mention that while abroad, Dr. Grady purchased me a birthday cake and sang "Happy Birthday", a memory that I truly cherish.

Special recognition needs to be given to my current roommate, Nicholas Toliver, for frequently lending his ear to my research woes. He has selflessly spent countless hours discussing aspects of my research with me and has provided unique insight in

more than one occasion. Nick has contributed plenty of time, energy, and perspective on my research to warrant being a co-author, but he said that he would be willing to settle for a formal acknowledgment.

Table of Contents

List of Figures

Abstract

A classical molecular dynamics simulation was conducted in order to determine the extent of surfactant adsorption on zwitterionic functionalized Al_2O_3. Sodium dodecyl sulfate was used as a model anionic surfactant, and carboxybetaine methacrylate was used as the zwitterionic material that functionalized half of the alumina surface. The amount of surfactant that adsorbed on the zwitterionic functionalized side was compared to the amount of surfactant adsorbed on the pristine portion of the alumina. The zwitterionic functionalized portion of the alumina surface exhibited enhanced surfactant adsorption, which is mainly due to the configurations of the positive and negative moieties relative to the alumina surface. Factors involving the electrostatic nature of the alumina surface and the flexibility of the zwitterion were discussed. It is also worth noting that the first water layer on top of the alumina surface adsorbs to the surface more strongly than the surfactant anion. The effects of the initial configuration on the surfactant self-assembly process is examined. Several avenues of continued efforts are suggested for future research related to this project.

Chapter 1: Introduction

In the current state of the oil industry, enhanced oil recovery (EOR) techniques are crucial to maximizing the production from active wells thus mitigating the need to expend capital on drilling new wells. EOR aids in the depletion of a reservoir by assisting in recovering more oil from the pore structure within the reservoir formation, which is normally left in place by traditional production methods.

1.1. Surfactant Flooding

One method of EOR is the chemical injection of surfactants into the oil reservoir in order to decrease the oil/water interfacial tension thereby improving the mobility of the oil trapped within the reservoir pores. [1] In these surfactant flooding processes, loss of the injected surfactant to adsorption on the reservoir rock limits the economic viability of this EOR method. In an effort to reduce the adsorption of surfactant on the surface, sacrificial agents are sometimes utilized in order to change the surface chemistry of the rock. One such method is using sacrificial alkali which can effectively tune the electrostatic interactions at the surface, thereby reducing the adsorption of anionic surfactants. A significant drawback to using sacrificial alkali is that in the presence of anhydrite in the reservoir rock composition the alkali will react, thus preventing the decrease of surfactant adsorption. [2] Other sacrificial agents exist, such as polyelectrolytes, which do not suffer from the same drawback. However, even polyelectrolytes are ineffective in certain situations such as high salinity conditions or when significant quantities of divalent ions are present in the reservoir environment.

1.2. Zwitterionic Materials

Zwitterions are characterized by possessing both cationic and anionic moieties within the same molecule. The presence of electrostatically juxtaposed elements within the same molecule can promote a strong shell of hydration around zwitterionic materials in aqueous environments. As a result of the strong hydration, zwitterionic materials have been shown to exhibit non-specific resistance to protein adsorption, immunological responses, as well as biofilm formation. [3-6] These applications of zwitterionic materials inspired the concept that zwitterions could coat a reservoir wall to provide non-specific resistance to surfactant adsorption.

1.3. Research Approach

In order to investigate the interaction between zwitterionic materials and the anionic surfactants conventionally used in EOR while simultaneously probing the effects on surfactant adsorption, computational simulations via molecular dynamics have been applied to seek a fundamental understanding of these processes. Molecular dynamics simulations describe the propagation of a system through time and space. An initial configuration of particles is established with prescribed interactions, and then Newtonian equations of motion are integrated over a time step, typically on the order of femtoseconds, to sample the evolution of the system. By utilizing molecular dynamics, the dynamic interplay between surfactants, the zwitterionic material, and the surface can be analyzed to reveal whether zwitterionic materials are good candidates for controlling surfactant adsorption at surfaces.

Chapter 2: Simulation Methodology

2.1. Chemical Species

2.1.1. Sodium Dodecyl Sulfate

To model an anionic surfactant, sodium dodecyl sulfate (SDS), is chosen for the extensive amount of literature available for comparison regarding both the experimental and computational fields. A hydrogen-implicit model for SDS was chosen specifically to work well for interfacial interactions, as parametrized by Sun et al. [7] The SDS model established by Berkowitz et al. acts as the foundation for the head group of the Sun model which tunes the van der Waals interactions of the head group to better reproduce experimental interfacial values. [8]

2.1.2. Aluminum Oxide

In order to model the surface of a reservoir formation highly attractive to an anionic surfactant, aluminum oxide (0001) was utilized. This crystalline alumina model is terminated with aluminum atoms, providing a partial positive charge on the surface of the substrate for the dodecyl sulfate anions (DS) to readily adsorb to. The alumina is not hydroxylated, acting as a pristine surface. The aluminum and oxygen atoms in the alumina are held in fixed positions throughout the course of the simulation in order to reproduce better water properties at the surface as shown by Striolo et al. [9] The Coulombic and van der Waals interactions are described by the ClayFF forcefield. [10]

2.1.3. SPC/E Water

The SPC/E water model is chosen for its compatibility with the SDS and alumina model utilized in this work. [11] SPC/E water is a rigid, non-polarizable model which is less computationally expensive compared to flexible, polarizable models, and the SPC/E model has a good reputation amongst people performing simulations of water. [12]

2.1.4. Carboxybetaine Methacrylate

The use of carboxybetaine methacrylate (CBMA) as the simulated zwitterionic material is heavily influenced by the computational and experimental work of Jiang et al. on the anti-fouling properties of CBMA and related zwitterionic moieties. [13-16] In contrast to the CVFF parameters and partial charge distribution implemented by Jiang et al., this work utilizes an OPLS-UA set of parameters with a complimentary set of partial charges and implicit hydrogens.

2.2. Molecular Dynamics

2.2.1. Overview

In classical molecular dynamics, a chemically unreactive collection of particles interacts through Coulombic and van der Waals potentials. Once the forces between particles are calculated from the potentials, Newtonian equations of motion are then integrated for a given time step, usually on the order of one femtosecond. Bonded interactions include bond stretching, angle bending, and torsional interactions. Comparatively, the non-bonded interactions involving the Coulombic and van der Waals potentials consume

drastically more computational resources than the bonded interactions. In an effort to reduce the computational expense of the non-bonded interactions, relatively short-range potentials, that is, the van der Waals interactions, are truncated at a certain distance commensurate with an appropriate level of accuracy warranted in the simulation.

To avoid artificial walls and finite size effects, periodic boundary conditions (PBC) are applied to the system being simulated. While PBC are implemented, particles passing through a boundary of the simulation cell reappear on the opposite side of the simulation cell. Non-periodic boundary conditions are possible to implement, but can be significantly more computationally expensive due to the algorithms used in long-range electrostatic solvers.

2.2.2. Parameters and Potentials

The *LAMMPS* molecular dynamics software package was used to perform the simulations in this work, specifically the Feb. 16, 2016 release. [17] A constant volume simulation box of dimensions 16.5 nm x 9.4 nm x 13.5 nm was used in the simulation. The temperature was kept constant at 298 K using a Nosé-Hoover thermostat. 3-D PBC were used and the simulation was allowed to run for 30 ns. The van der Waal forces between two particles, of type i and j, were represented with a Lennard-Jones (LJ) potential using a 1.4 nm cutoff:

$$E_{LJ} = 4\epsilon_{ij}\left[\left(\frac{\sigma_{ij}}{r_{ij}}\right)^{12} - \left(\frac{\sigma_{ij}}{r_{ij}}\right)^{6}\right] \quad (2\text{-}1)$$

where ϵ_{ij} is the depth of the potential well, σ_{ij} is the distance at which the particle-particle potential is zero, and r_{ij} is the distance between the two particles. The epsilon and sigma values for each i-j interaction are computed using the Lorentz-Berthelot mixing rule. The r^6 term has physical meaning associated with the attractive van der Waals forces while the r^{12} term functions as the repulsive term and it is computationally efficient to model as the squared value of the r^6 term. The 1.4 nm cutoff for the LJ potential is used in order to comply with the forcefield parameterization described by Sun et al. for the SDS model.

The Coulombic forces between charged particles i and j are calculated without any cutoff, thus allowing for long-range electrostatic phenomena to be simulated:

$$E_{Coul} = \frac{Cq_iq_j}{\epsilon_D r_{ij}} \tag{2-2}$$

where C is an energy-conversion constant, q_i and q_j are the charges on the interacting particles, and ϵ_D is the dielectric constant. In order to efficiently compute the long-range electrostatic interactions between particles, the particle-particle particle-mesh (PPPM) solver is invoked. This PPPM long-range electrostatic solver uses a 3-D mesh to map point charges, then solves Poisson's equations using a 3-D fast Fourier transform algorithm, interpolating the electric field onto the atoms on the 3-D mesh. [18]

The interactions between two directly bonded particles are simulated with a harmonic bond potential which utilizes an equilibrium bond distance and an associated energy penalty for deviating from that equilibrium distance:

$$E_b = K_b(r - r_0)^2 \tag{2-3}$$

where K_b is the energy penalty per distance squared, representing the strength of the bond. The equilibrium bond length is r_0 while the actual distance between the two bonded particles is r.

Similarly, the bonded interactions between three particles that constitute an angle are also represented with a harmonic angle potential which utilizes an equilibrium angle value and an associated energy penalty for deviating from that equilibrium angle value:

$$E_\theta = K_\theta(\theta - \theta_0)^2 \quad (2\text{-}4)$$

where K_θ is the energy penalty per radian squared, representing the degree of flexibility of the angle. The equilibrium angle is θ_0 while the actual angle between the three particles is θ.

The torsional interactions are calculated using a Fourier potential:

$$E_\phi = \sum_{i=1,m} K_i[1.0 + cos(n_i\phi - d_i)] \quad (2\text{-}5)$$

where m is an integer value greater than or equal to 1; K_i is an energy constant; n_i is an integer value greater than or equal to 0; d_i is in units of degrees; and ϕ is the calculated dihedral angle also in units of degrees.

In order to maintain planarity of the terminal carboxylate group on the CBMA molecules, an improper dihedral potential is taken into account:

$$E_\psi = K_\psi[1 + dcos(n\psi)] \quad (2\text{-}6)$$

where K_ψ is the energy constant for the improper dihedral angle, d is either -1 or +1, and n is an integer value between 0 and 6, inclusive.

Non-bonded interactions are turned off for 1-2 and 1-3 interactions, where 1-2 and 1-3 denote the interactions between a particle and its first bonded and second closest bonded neighbors, respectively. For 1-5+ interactions, particles that are four bonds and further away have their non-bounded interactions fully incorporated into the energy calculation. The intramolecular 1-4 non-bonded interactions are more complex, utilizing scaling factors with regards to how much of the LJ and Coulombic interactions are included. For the OPLS-UA parameters used for the CBMA, scaling factors of $\frac{1}{8}$ and $\frac{1}{2}$ are used for the LJ and Coulombic 1-4 non-bonded interactions, respectively. For the dodecyl portion of the SDS molecules, the TraPPE forcefield is used in the Sun et al. model for SDS, which uses scaling factors of zero, or in other words, turns off the 1-4 non-bonded interactions. Also in accordance with the Sun et al. SDS model, the head group of the SDS molecule utilizes scaling factors of $\frac{1}{2}$ and $\frac{5}{6}$ for the LJ and Coulombic interactions, respectively.

Utilizing incorrect 1-4 non-bonded scaling factors can produce drastically different results than intended for a forcefield. Example simulations are shown below where the dodecyl chains of the SDS molecules are simulated with all other conditions held similar expect for the 1-4 non-bonded scaling factors. Figure 1 is the simulation utilizing the TraPPE scaling factors as the Sun et al. model intended. Figure 2 shows the simulation in which the head group scaling factors are applied, drastically affecting the dodecyl configurations. The dodecyl configurations in Figure 2 are not representative of

experimental observations, thus illustrating the importance of correctly implementing the 1-4 non-bonded scaling factors intended to be used for a particular forcefield.

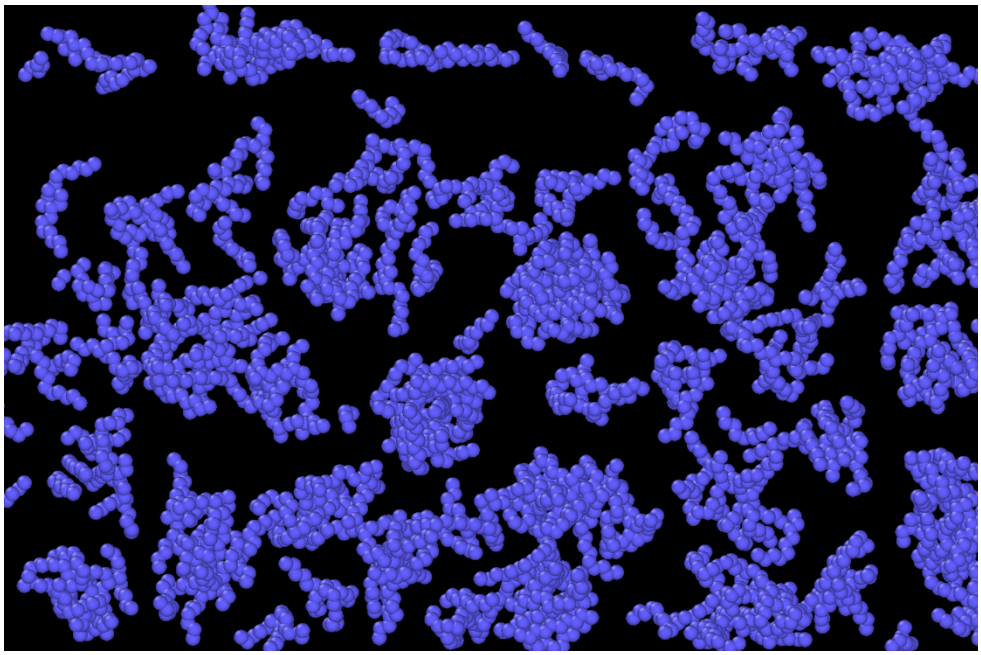

Figure 1: Correct 1-4 non-bonded scaling factors applied.

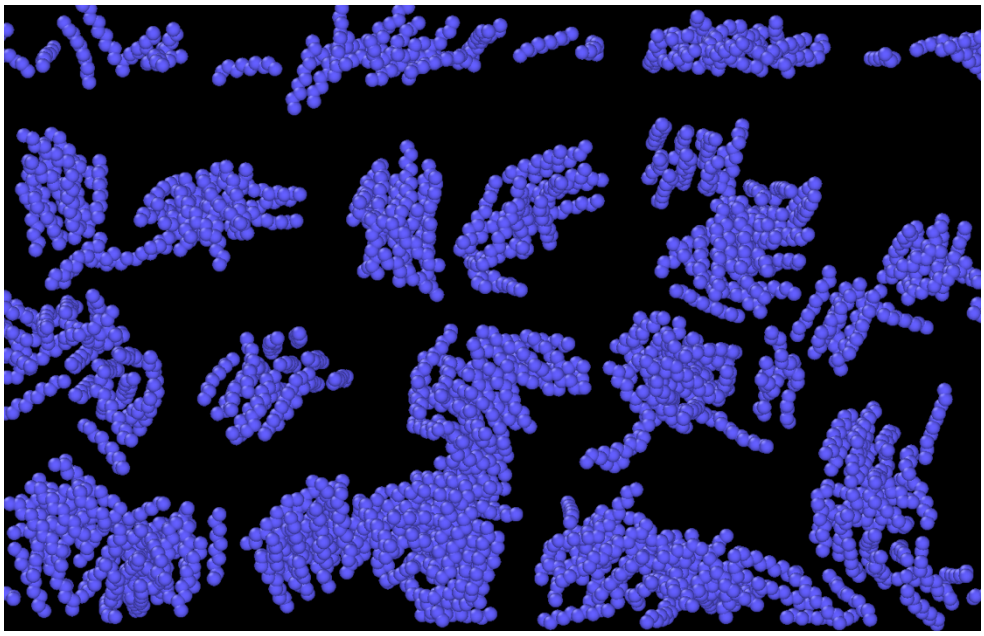

Figure 2: Incorrect 1-4 non-bonded scaling factors applied.

2.3. Initial Configuration

The Al_2O_3 (0001) substrate used as the primary surface for surfactant adsorption is simulated using a 16.5 nm x 9.4 nm x 2.55 nm slab consisting of 48,000 atoms. These alumina atoms are held fixed in their exact coordinates over the course of the simulation, meaning that bonded and non-bonded interactions between alumina atoms are turned off through commands in LAMMPS. The aluminum oxide is terminated by aluminum atoms, exposing a partial positive charge on the surface.

There are 15 CBMA molecules attached to one half of the alumina surface. The artificial bond connecting the CBMA to the rigid aluminum atoms is intended to prevent the zwitterionic moieties from diffusing away from the surface. The CBMA molecules are initially in a vertical configuration, perpendicular to the plane of the alumina surface, with the negatively charge moiety the furthest away from the substrate. Having only half of the alumina functionalized with the zwitterionic material allows for simultaneous comparison to the non-functionalized surface, as depicted in Figure 3.

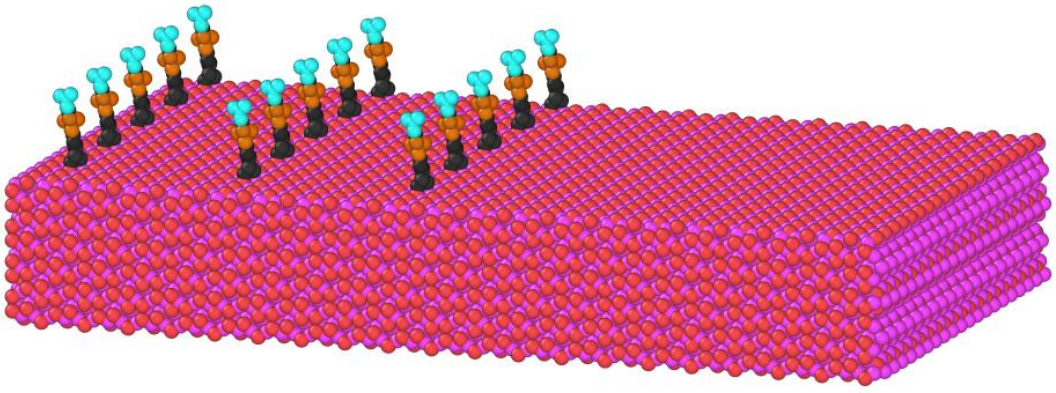

Figure 3: CBMA functionalized alumina surface, negative CBMA moiety (blue), positive CBMA moiety (orange), aluminum (red), oxygen (pink).

To place 46,000 water molecules and 400 SDS molecules into the simulation box with an initial random configuration, the *PACKMOL* software was utilized. [19] The water molecules were initially placed in column above the entire alumina surface starting just a few angstroms above the top layer of aluminum atoms. The SDS molecules were placed, with the sodium counterion initially beside the sulfate head group, in the same column as the water, except starting 2 nm above the surface to avoid spurious interactions with the CBMA molecules.

The initial configuration was relaxed by briefly using a reduced time step value of 0.01 fs before carrying out the remainder of the calculations using a 1 fs time step. After this brief relaxation of the system from the initially random orientation of the particles, the liquid column extended above the surface approximately 10 nm. The remainder of the simulation cell height previously given, was occupied by a 10 nm vacuum. This vacuum helped provide a buffer region so that 3-D PBC could be used for computational efficiency while minimizing the effects of the periodic images along the dimension corresponding to the normal of the alumina surface.

Chapter 3: Results

3.1. Enhanced Surfactant Adsorption

The distribution of the sulfur atom in the DS anion with respect to distance from the surface can be used to approximately evaluate the extent of adsorption on different parts of the alumina surface. The following set of graphs provided in Figure 4 compare the surfactant distribution over the entire surface to the distributions on each half of the alumina surface, zwitterionic functionalized and pristine, while also providing a plot to indicate adsorption evolution over time.

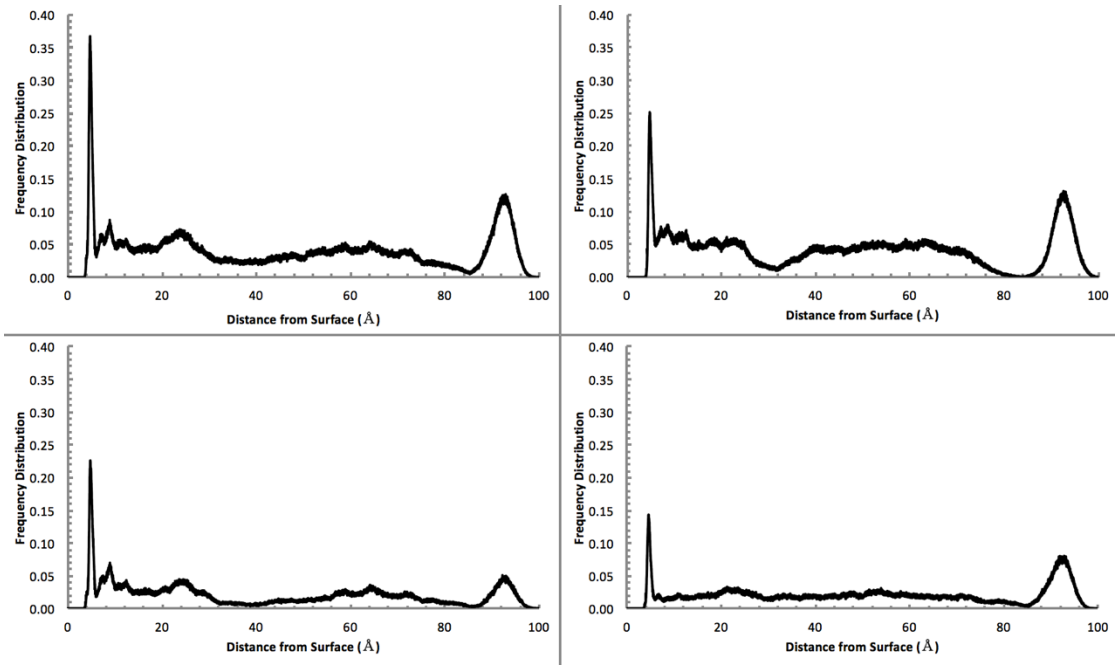

Figure 4: Sulfur frequency distribution for variable distance away from the alumina surface, entire surface 29-30 ns (top left), entire surface 20-21 ns (top right), CBMA side 29-30 ns (bottom left), pristine side 29-30 ns (bottom right).

In Figure 4, every plot displays a sharp peak 0.5 nm above the surface indicating adsorption of the DS anion to the partially positive alumina surface. In addition, the CBMA functionalized side of the alumina actually has enhanced adsorption of surfactant compared to the non-functionalized, pristine part. Visually assessing the distribution of the surfactant molecules can be helpful and a snapshot of the system at 30 ns is provided in Figure 5.

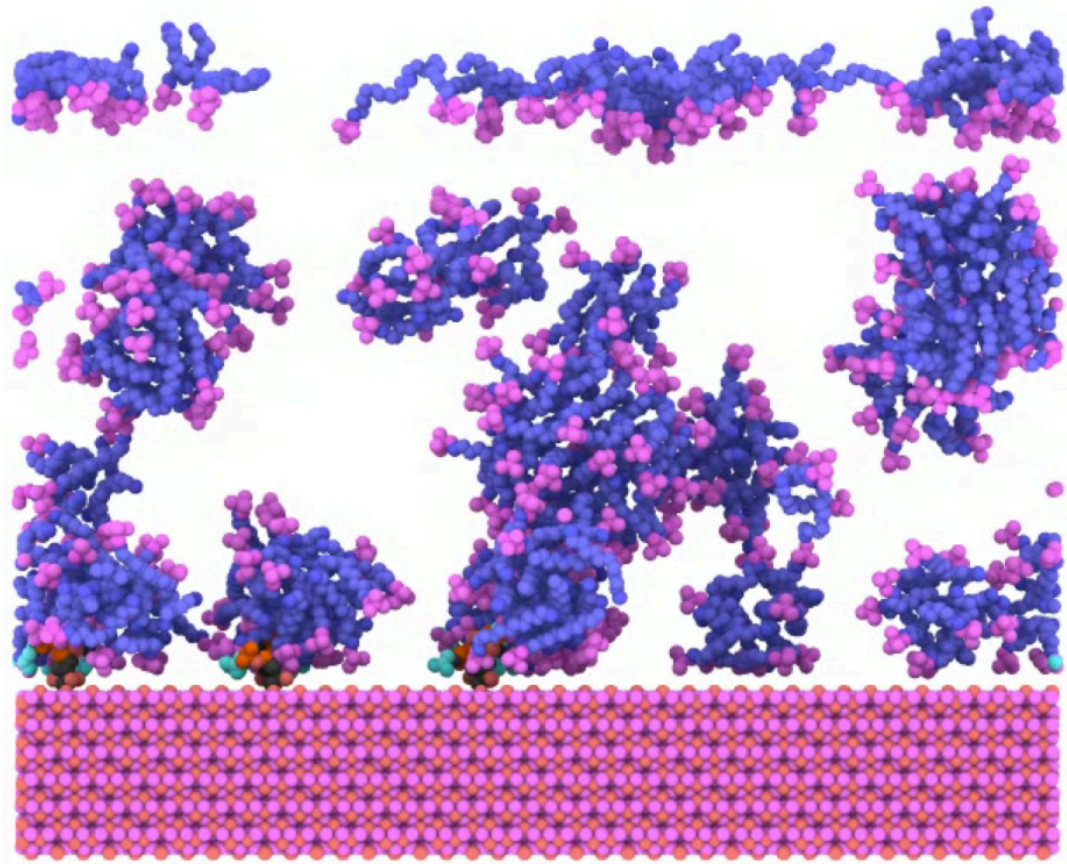

Figure 5: System after 30 ns of simulation, water omitted for clarity.

Immediately, the difference in extent of surfactant adsorption is obvious between the zwitterionic functionalized side and the pristine portion of the alumina

surface. Figure 6 illustrates the behavior that was expected to occur in the system, where the zwitterionic groups create a strong layer of hydration as described by Schlenoff, thus acting as a hindrance to surfactant molecules diffusing into that space. [20] This hydration layer then prevents the SDS from adsorbing to these alumina sites surrounded by zwitterionic functional groups. The observed behavior of the system can be divided into four primary regions and is presented graphically in Figure 7.

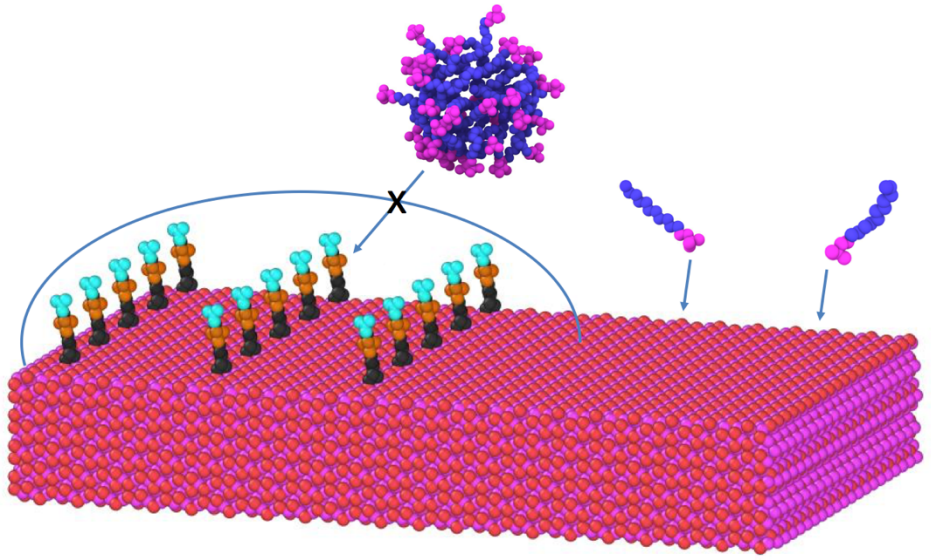

Figure 6: Expected behavior of CBMA functionalization, blue curve indicates proposed strong layer of hydration.

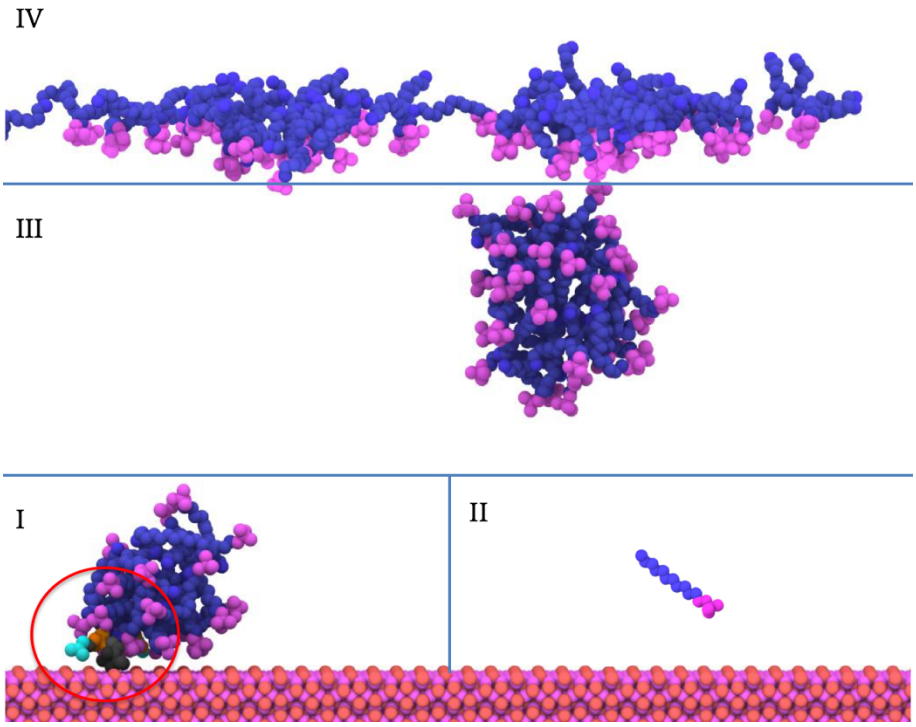

Figure 7: Regions of surfactant distribution: region I is for enhanced adsorption by CBMA; region II is for relatively less adsorption on the pristine side; region III is the bulk fluid; region IV is the water-surfactant-vacuum interface. Red circle indicates CBMA location.

The difference between surfactant adsorption in region I and II in Figure 7 is a result of the spatial configuration of the CBMA molecules. The simulated CBMA molecules are flexible enough that the negative carboxylate moiety on the terminal end of the CBMA structure is capable of bending over to stay closer to the alumina surface. This situation is electrostatically favorable since the negatively charged carboxylate group becomes closer to the partially positive alumina surface. While the negative moiety is bending over and getting closer to the surface, the positive moiety is becoming increasingly exposed to the bulk fluid, attracting the anionic surfactants. The strong layer of hydration expected around the zwitterions is likely being disrupted by the

significant interactions between the alumina surface and the negative moiety on the CBMA molecules. The positive surface charge is attracting the carboxylate group on the CBMA, reducing the effects of the zwitterionic hydration since there is a locally higher amount of positive charge disrupting the balanced electrostatic interaction between the CBMA moieties. This proposed explanation of the behavior observed in the simulation is illustrated below in Figure 8.

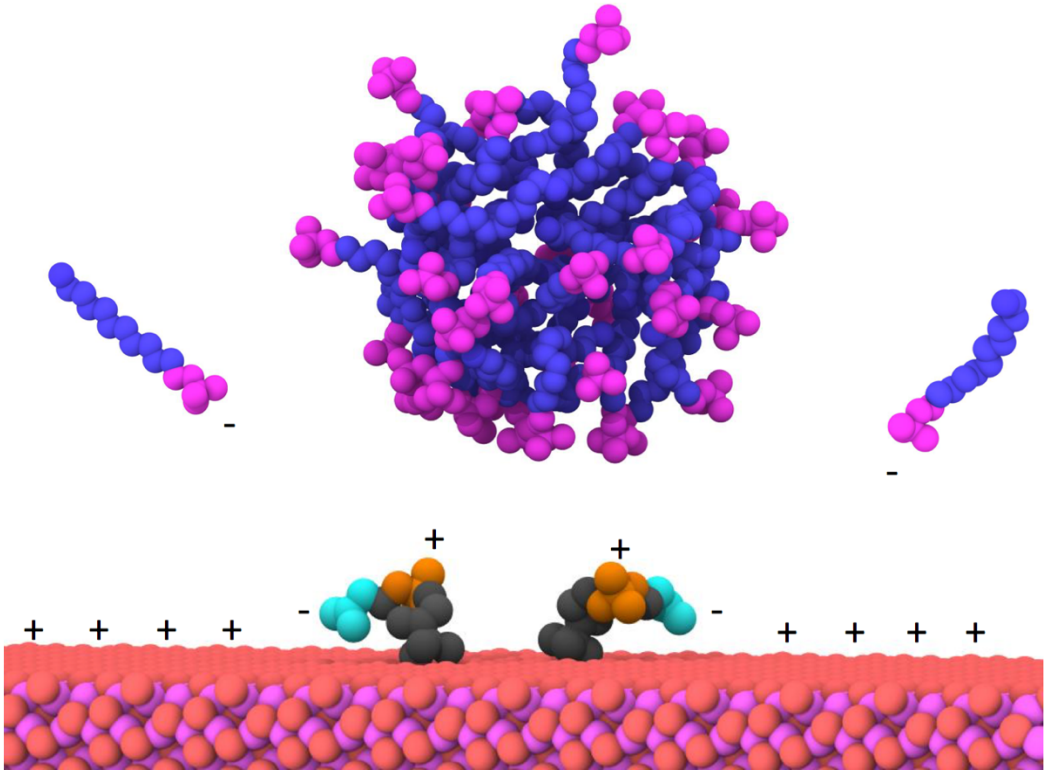

Figure 8: Proposed explanation of enhanced surfactant adsorption by CBMA.

3.2. First Water Layer

It has been reported that water dissociatively chemisorbs on a pristine aluminum oxide surface, coating the surface with hydroxyl groups. In our system, since the CBMA carboxylate groups preferentially interacts with the surface, it is worth studying how water/surface interactions will be affected. As shown in Figure 9, the distance of

hydrogen and oxygen atoms from the surface reveals that there is a clearly defined first water layer above the surface between 0.0-2.5 Å. In region I, the integral of the hydrogen distribution (black line) is approximately twice the value of the integral of the oxygen distribution (red line). This makes sense as there are twice as many hydrogen atoms as oxygen atoms for a given quantity of water molecules. Even without the comparison of integrating the curves, the oxygen curve in region I clearly shows significant definition in the presence of a single water layer simply by the distribution of the oxygen atoms in the water molecules. The overall trend of the graph is that the structure of water is significantly altered in regions I and II, but quickly approaches the characteristics of bulk water once in region III. The structure of the first water layer can also be visualized, see Figure 10. There is an identifiable strip of oxygen atoms between two rows of hydrogen atoms. Such a pattern confirms the observed peaks of region I in Figure 9, indicating an ordered first layer of water. A top-down view of that first layer of water is also provided in Figure 11.

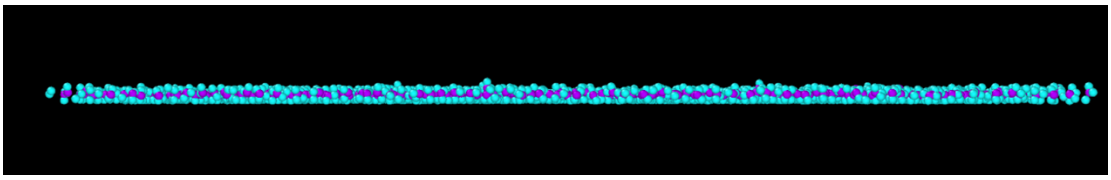

Figure 9: Side profile of first water layer, oxygen (purple), hydrogen (blue).

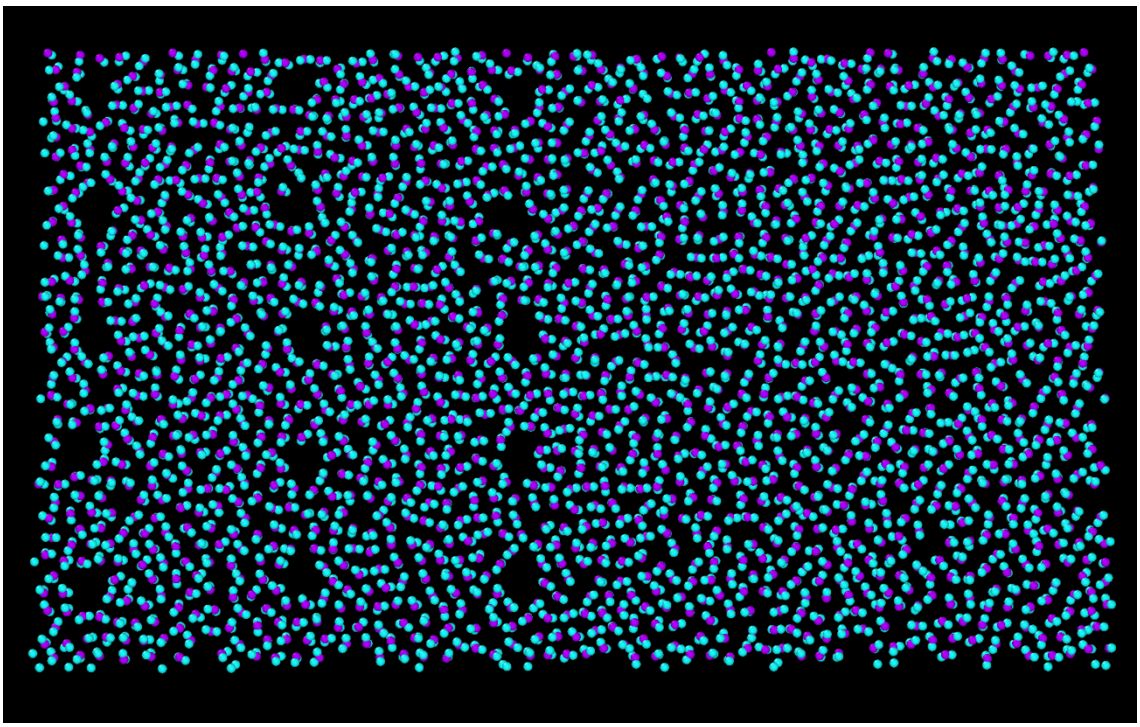

Figure 10: Top-down view of the first water layer, vacancies on left side are from CBMA groups, oxygen (purple), hydrogen (blue).

While the presence of a first water layer has been identified, it is of interest to analyze the orientations of water molecules in this first water layer. In order to assess the orientation of the water molecules, the orientation of their dipoles will be evaluated: the individual O-H vectors are calculated to illustrate the direction in which the dipole points. The convention used here is that the dipole points in the direction of negative charge on the molecule. As shown in Figure 12, for the rigid SPC/E water model, the dipole points away from the hydrogen atoms and toward the oxygen atom along the axis of symmetry for the molecule.

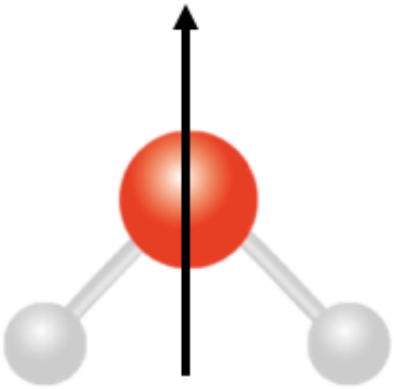

Figure 11: Dipole Convention.

With this convention, we can analyze the orientation of water with respect to the surface: identify the intersection of the dipole with the surface, and measure the angle between the dipole vector and the alumina surface. This angle acts as an orientation parameter. If the dipole is pointing toward the surface, that angle will be negative. If the dipole is pointing away from the surface, that angle will be positive. If the dipole is parallel to the surface, that angle will be zero. Using the convention and procedure mentioned above, the orientation of the first water layer is plotted in Figure 13.

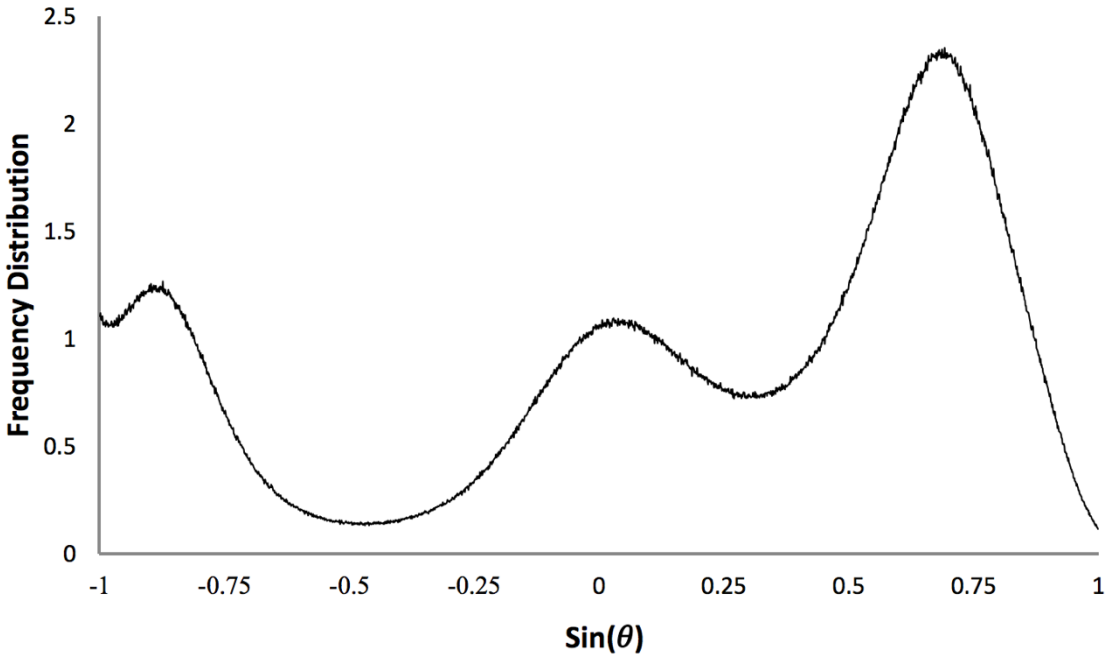

Figure 12: Water dipole distribution, negative values indicate dipole pointing toward the surface, positive values indicate dipole pointing away from the surface.

The configurational trends seen in Figure 13 are not entirely unambiguous. This is because water molecules can rotate around their axis of symmetry and maintain the same dipole orientation. In other words, there is ambiguity about the relative location of the hydrogen atoms for a given molecule of water with respect to the surface. In order to obtain this piece of information, the relative difference between hydrogen atoms and the alumina surface for a given water molecule is calculated and then paired with the same dipole orientation parameter calculated in Figure 13. Such analysis results in an array populated with information about how frequent each possible combination

of dipole orientation and relative hydrogen distance to the surface is. This array is presented in the form of a greyscale heat map in Figure 14.

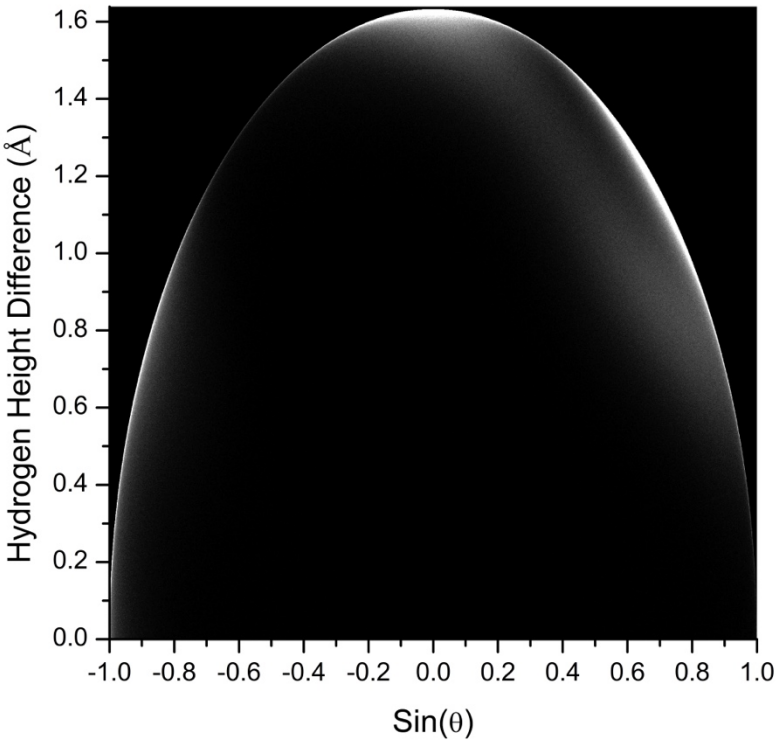

Figure 13: Frequency distribution of water molecules possessing a certain combination of x-axis and y-axis values, more frequent (white), less frequent (black).

Figure 14 shows that there is not a significant amount of water molecules with a zero dipole value and a small hydrogen height difference. In other words, there is a distinct lack of water configurations where the plane of the water molecule is parallel to the plane of the alumina surface. Another way to phrase this result is that there are

hardly any water molecules present in the first water layer which do not have at least one O-H significantly oriented to either the alumina surface or the second water layer.

Further analyzing Figure 14, the high frequency distribution on the left side of the plot indicates that there is a significant amount of water molecules which have both of their O-H bonds pointing toward the second water layer. The hotspots in the middle and right side of Figure 14 indicate that these configurations have one O-H pointing toward the alumina surface and the other pointing toward the second water layer. A slight discrepancy can be made between the middle and right side hotspots in that the middle hot spot possesses the highest degree of separation between hydrogen atoms within a given molecule when compared in the direction normal to the surface. This is potentially significant because both middle and right side hotspot configurations have their hydrogens point toward the surface and are at the same relative distance from the surface. This is also evident from the first large peak presented in the hydrogen curve in Figure 9. If both the middle and right hotspots in Figure 14 have the same hydrogen position for one O-H segment, in terms of distance from the surface, then that would mean that the right side hot spot would have an O-H segment with a hydrogen significantly closer to the other atoms in the first water layer compared to the middle hotspot. A way to physically comprehend this difference is that the middle hot spot is likely more engaged in hydrogen bonding with the second water layer, while the right hot spot in Figure 14 is more likely to hydrogen bond with other members of the first water layer with the O-H segment pointing slightly away from the surface.

3.3. Second Water Layer and Surfactant Adsorption

Evidence from region II in Figure 9 as well as the potential water configurations identified through Figure 14 indicate that there is significant interaction between the first and second water layers. A similar analysis to Figure 13 was conducted on the second water layer to reveal trends in the dipole orientation and is presented in Figure 15.

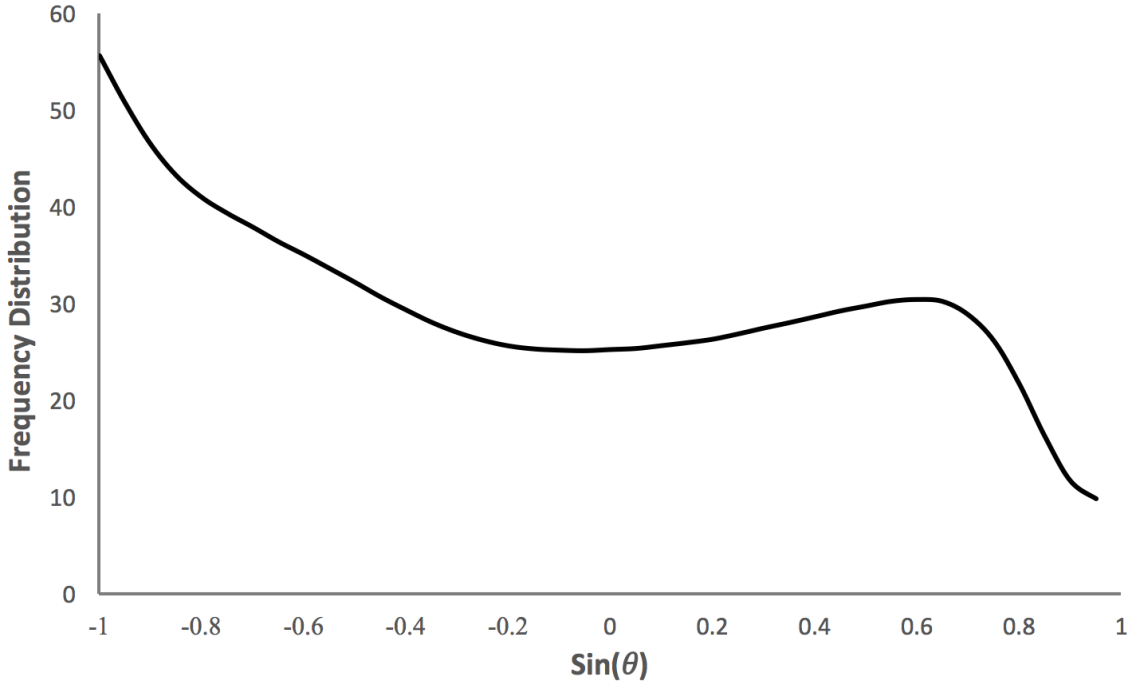

Figure 14: Second water layer dipole distribution: negative values indicate the dipole is pointing toward the surface, while positive values indicate the dipole is pointing away from the surface.

From Figure 15 it is clear that there is a preference for water to have a negative dipole value. This means that there are a significant number of water molecules in the second water layer that have their oxygen pointed down toward the first water layer and both of their O-H segments pointing away from the first water layer. This fits well

into the narrative that the first water layer proposed since there was a significant amount of O-H segments in the first water layer pointing toward the second water layer. The presence of these elements in the first and second water layers provides evidence for hydrogen bonding between the two layers, although the adsorption of the first water layer to the alumina surface is likely the dominating interaction for the first layer of adsorbed water.

So far, the presence of the surfactant has not been discussed in relation to the structural trends of the first and second water layers. When comparing the x-axis values of the adsorption peaks in Figure 4, it seems that the head group of the DS anion is residing between the first and second water layers. While the actual x-axis values read from Figure 4 would indicate a higher position, the additional length of the oxygens in the sulfate head group need to be accounted for since Figure 4 only reveals information about the distribution of the positions of the sulfur atoms in the system. When this discrepancy is accounted for, the head group is then confirmed to reside just above the first water layer. Visualization also corroborates this phenomenon, showing that the anionic head group never penetrates the first water layer. To confirm that both the CBMA and SDS have minimal effect on the structure of the first water layer, a 5 ns simulation was performed using the same alumina substrate with water molecules, but no SDS or CBMA molecules. The same analysis was conducted on this first water layer, revealing the same trends which were almost identical to the corresponding results from the system containing SDS and CBMA.

This implies that the strength of the adsorption of water directly adsorbed to the alumina is potentially a stronger interaction than the sulfate head group directly adsorbed to the alumina surface. The adsorbed water molecules also have the additional consideration of the hydrogen bonding network that is formed with the surrounding molecules in the first and second water layers. In order for the sulfate anion to pass through the first water layer, the ion would have to overcome the electrostatic repulsion from the very concentrated layer of oxygen atoms at the first water layer as indicated by the distinct peak of the red curve in region I of Figure 9.

3.4. SDS Morphology

Conventional surfactant knowledge suggests that SDS monomers are expected to adsorb to interfaces, forming at least a monolayer, before micelle formation occurs. However, in this system there are mostly aggregates seen at the alumina interface and relatively few monomers. This is a significantly different from what is experimentally observed in typical surfactant adsorption processes. One possible explanation for this occurrence is that at 30 ns, the simulation is not at equilibrium. Comparison of the upper quadrants of Figure 9 indicate that the system is not at equilibrium because the amount of surfactant adsorbed at the alumina interface is increasing over time. Figure 16 shows the distribution of aggregate sizes in the system at 30 ns, with the criteria defining what constitutes an aggregate being taken from Sammalkorpi et al. [21] The largest aggregate size seen in Figure 16 is 39 monomers. This is significantly smaller than the expected equilibrium aggregate size, especially for the relatively high concentration of SDS

present in the system. Indeed, coarse-grained models of random SDS self-assembly into micelles have shown that it takes almost 300 ns to form aggregates of a stable size corresponding to the concentration of surfactant in the system. [22] Using classical molecular dynamics with an atomistic system, reaching 300+ ns for a system of the size simulated in this work is currently not computationally tractable within a couple months. In order to access larger time scales, either a different system design needs to be employed, or additional modeling techniques such as coarse-graining methods need to be implemented.

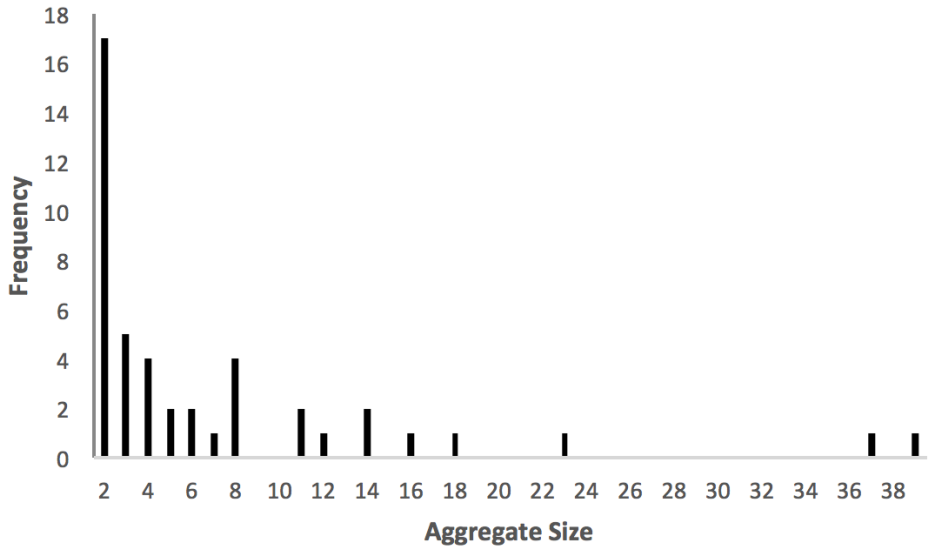

Figure 15: Aggregate size in terms of number of constituent monomers, 30 ns into simulation.

The other aspect to inspect is the immediate entropic considerations for the initial configuration of the system. The transition from monomers to micellar aggregates occurs when the configurational entropy of the aggregate becomes larger compared to the translational entropy of the monomers. As SDS concentration increases, the

translational entropy decreases. In the initial configuration of the system, the concentration is high enough to immediately promote the formation of aggregates. There is competition between the translational entropy of the monomers and the entropy gained when micelles are formed by reducing the number of water molecules surrounding the hydrophobic tail of the surfactant molecules in a highly ordered fashion. [23] The surfactant concentration that balances these two competing forms of entropy is the critical micelle concentration (CMC) and can be expressed mathematically:

$$\mu = \mu_N^0 + \frac{k_B T}{N} \ln\left(\frac{f_N X_N}{N}\right) \quad (3\text{-}1)$$

$$f_N X_N = N\left[f_1 X_1 e^{\frac{\mu_1^0 - \mu_N^0}{k_B T}}\right]^N \quad (3\text{-}2)$$

$$(X_1)_{CMC} \approx e^{\frac{\mu_N^0 - \mu_1^0}{k_B T}} \quad (3\text{-}3)$$

where μ is chemical potential; T is temperature; k_B is the Boltzmann constant; μ_N^0 is the mean interaction free energy in the aggregate; N is the aggregation number; f_N is the activity coefficient, and X_N is the volume fraction of amphiphiles in an aggregate of size N. [24]

Chapter 4: Future Research Plans

4.1. CBMA Coverage

With the result of enhanced surfactant adsorption at the CBMA-alumina interface, it is an obvious goal to test other materials and conditions to try to achieve decreased surfactant adsorption on zwitterionic functionalized alumina. Even if CBMA continues to be the zwitterionic material of choice, there are several parameters that could significantly affect the out come of the adsorption trends. The density of the CBMA on the surface could play an enormous role in how effective the zwitterion is in repelling surfactant adsorption. At higher density coverages, it is reasonable to expect that the CBMA molecules would maintain a more rigid and vertical character. This would be due to the carboxylate head groups of neighboring CBMA molecules acting as electrostatic barriers to bending over so that the negative carboxylate moiety could get closer to the partially positive alumina surface. The sheer steric hindrance of having closer packed CBMA molecules could also ensure that the negative moiety does not become occupied with the surface. Indeed, closer packing of the CBMA molecules could result in the interstitial water also being more difficult to relocate, thus decreasing the effective flexibility of the CBMA molecules attached to the alumina surface.

4.2. Electrolyte Concentration

The impact of electrolyte concentration is another crucial factor in most ionic surfactant systems. The effect of swamping electrolyte on the interplay between CBMA and anionic surfactants has not been investigated, but could yield interesting results. There is the

potential that high salinity environments could render the zwitterionic material less effective at preventing surfactant adsorption, but the opposite could potentially be true as well. The presence of high concentrations of electrolyte could aid in the creation of a strong layer of hydration that repels the adsorption of surfactant molecules to the surface. There was also a small amount of evidence in the data collected during this work, that the sodium ions from the SDS were adsorbing more strongly to the alumina surface than even the water. Over time the number of sodium ions slightly increased at the alumina interface while the number of adsorbed water molecules slightly decreased, indicating that the sodium ions were competitively adsorbing with the water molecules. It is possible that at a high enough ion concentration, the number of adsorbed ions on the alumina surface would begin to exhibit Langmuirian adsorption trends and ultimately act as electrostatic inhibitors to further ion adsorption at the alumina surface. The effect of the size of the ion could also be computationally studied as well as the effect of multivalent ions on the surfactant aggregates at the alumina interface as studied experimentally by Harwell and Bitting. [25]

4.3. Hydroxylated Alumina

Realistically, any aluminum oxide in an aqueous environment is going to dissociatively chemisorb water molecular to form a layer of hydroxyl groups on the surface of the alumina. These functional groups were not taken into account in this work, but could easily be the focus of continued efforts on this project. Differences between the water structures in the first layer of water between hydroxylated alumina and pristine alumina

have already been investigated by Striolo et al. [26] This potentially indicates that the extent of hydroxylation on the surface could impact the adsorption of anionic surfactants since the first water layer seemed to be an obstacle preventing the anionic surfactant in this work from getting closer to the alumina surface. The interactions between the CBMA molecules, or any zwitterionic material, with the hydroxyl groups on the surface of the aluminum oxide could be a potential avenue of exploration. It is possible that the hydroxyl groups could electrostatically interact with both the positive moieties and negative moieties that a zwitterionic material could have.

4.4. Accessing Larger Time Scales and Rare Events

One of the most challenging aspects of modeling surfactant systems computationally is that the time scale on which the molecules self-assembly, typically several hundred nanoseconds, is at the edge of what is realistically feasible to simulate. Pending a numerical computing revolution, non-classical, non-atomistic methods for performing molecular dynamics simulations are necessary to investigate the dynamic process of surfactant self-assembly processes including the formation of monolayers, bilayers, and micelles. Coarse-graining is a technique used to access much longer time scales at a reduced computational expense, but inherently lacks atomic detail. Observing the process of surfactant monomers desorbing from a surface, or the process of monomer exchange in micelles is very challenging as these are rare events. Rare events could happen once every few hundred nanoseconds, so it is not practical to try to collect data on these rare events through conventional simulation techniques. Advanced sampling

techniques such as forward flux sampling or umbrella sampling could potentially be used to garner useful information from these processes.

References

[1] Schramm, L. L. (2010) Surfactants: fundamentals and applications in the petroleum industry. Cambridge University Press Cambridge.

[2] Lopez-Salinas, J. L., Hirasaki, G. J., and Miller, C. A. (2011) Determination of Anhydrite in Reservoirs for EOR. SPE International Symposium on Oilfield Chemistry.

[3] Shao, Q., White, A. D., and Jiang, S. (2014) Difference of Carboxybetaine and Oligo(ethylene glycol) Moieties in Altering Hydrophobic Interactions: A Molecular Simulation Study. The Journal of Physical Chemistry B 118, 189–194.

[4] Yang, W., Xue, H., Li, W., Zhang, J., and Jiang, S. (2009) Pursuing "Zero" Protein Adsorption of Poly(carboxybetaine) from Undiluted Blood Serum and Plasma. Langmuir 25, 11911–11916.

[5] Keefe, A. J., and Jiang, S. (2011) Poly(zwitterionic)protein conjugates offer increased stability without sacrificing binding affinity or bioactivity. Nature Chemistry 4, 59–63.

[6] Zhang, L., Cao, Z., Bai, T., Carr, L., Ella-Menye, J.-R., Irvin, C., Ratner, B. D., and Jiang, S. (2013) Zwitterionic hydrogels implanted in mice resist the foreign-body reaction. Nature Biotechnology 31, 553–556.

[7] Cheng, T., Chen, Q., Li, F., and Sun, H. (2010) Classic Force Field for Predicting Surface Tension and Interfacial Properties of Sodium Dodecyl Sulfate. The Journal of Physical Chemistry B 114, 13736–13744.

[8] Dominguez, H., and Berkowitz, M. L. (2000) Computer Simulations of Sodium Dodecyl Sulfate at Liquid/Liquid and Liquid/Vapor Interfaces. The Journal of Physical Chemistry B 104, 5302–5308.

[9] Phan, A., Ho, T. A., Cole, D. R., and Striolo, A. (2012) Molecular Structure and Dynamics in Thin Water Films at Metal Oxide Surfaces: Magnesium, Aluminum, and Silicon Oxide Surfaces. The Journal of Physical Chemistry C 116, 15962–15973.

[10] Cygan, R. T., Liang, J.-J., and Kalinichev, A. G. (2004) Molecular Models of Hydroxide, Oxyhydroxide, and Clay Phases and the Development of a General Force Field. The Journal of Physical Chemistry B 108, 1255–1266.

[11] Berendsen, H. J. C., Grigera, J. R., and Straatsma, T. P. (1987) The missing term in effective pair potentials. The Journal of Physical Chemistry 91, 6269–6271.

[12] Vega, C., and Abascal, J. L. F. (2011) Simulating water with rigid non-polarizable models: a general perspective. Physical Chemistry Chemical Physics 13, 19663.

[13] He, Y., Tsao, H.-K., and Jiang, S. (2012) Improved Mechanical Properties of Zwitterionic Hydrogels with Hydroxyl Groups. The Journal of Physical Chemistry B 116, 5766–5770.

[14] Shao, Q., He, Y., White, A. D., and Jiang, S. (2010) Difference in Hydration between Carboxybetaine and Sulfobetaine. The Journal of Physical Chemistry B 114, 16625–16631.

[15] Shao, Q., and Jiang, S. (2014) Molecular Understanding and Design of Zwitterionic Materials. Advanced Materials 27, 15–26.

[16] Mahmud, G., Huda, S., Yang, W., Kandere-Grzybowska, K., Pilans, D., Jiang, S., and Grzybowski, B. A. (2011) Carboxybetaine Methacrylate Polymers Offer Robust, Long-Term Protection against Cell Adhesion. Langmuir 27, 10800–10804.

[17] Plimpton, S. (1995) Fast Parallel Algorithms for Short-Range Molecular Dynamics. Journal of Computational Physics 117, 1–19.

[18] Hockney, R., and Eastwood, J. (1988) Computer Simulation Using Particles.

[19] Martínez, L., Andrade, R., Birgin, E. G., and Martínez, J. M. (2009) PACKMOL: A package for building initial configurations for molecular dynamics simulations. Journal of Computational Chemistry 30, 2157–2164.

[20] Schlenoff, J. B. Zwitteration: Coating Surfaces with Zwitterionic Functionality to Reduce Nonspecific Adsorption. Langmuir 2014, 30 (32), 9625–9636 DOI: 10.1021/la500057j.

[21] Sammalkorpi, M., Karttunen, M., and Haataja, M. (2007) Structural Properties of Ionic Detergent Aggregates: A Large-Scale Molecular Dynamics Study of Sodium Dodecyl Sulfate. The Journal of Physical Chemistry B 111, 11722–11733.

[22] Pires, J. C. A. M., Moura, A. F. D., and Freitas, L. C. G. (2012) Investigating the spontaneous formation of SDS micelle in aqueous solution using a coarse-grained force field. Química Nova 35, 978–981.

[23] Liu, G., Wei, Y., Gao, F., Yuan, S., and Liu, C. (2016) Origins of entropy change for the amphiphilic molecule in micellization: a molecular dynamics study. Phys. Chem. Chem. Phys. 18, 11357–11361.

[24] Borówko, M. C. B. A. (2000) Computational methods in surface and colloid science. M. Dekker New York.

[25] Bitting, D., and Harwell, J. H. (1987) Effects of counterions on surfactant surface aggregates at the alumina/aqueous solution interface. Langmuir 3, 500–511.

[26] Argyris, D., Ho, T., Cole, D. R., and Striolo, A. (2011) Molecular Dynamics Studies of Interfacial Water at the Alumina Surface. The Journal of Physical Chemistry C 115, 2038–2046.

Appendix A: LAMMPS Input Script

```
# Initialization
units real
dimension 3
boundary p p p
atom_style full

read_data Al2O3-SDS-H2O-CBMA.data
#read_restart restart.100000

timestep  1.0
restart 50000 restart.*

# Structural Definition
# Pair Coeffs
#
# 1  Al
# 2  B
# 3  C
# 4  D
# 5  E
# 6  F
# 7  G
# 8  H
# 9  I
# 10  J
# 11  K
# 12  L
# 13  M
# 14  N
# 15  O
# 16  P
# 17  Q
# 18  R
# 19  S
# 20  T
# 21  U
# 22  V
# 23  W
# 24  X
# 25  Y
# 26  Z
```

Bond Coeffs
#
1 Al-G
2 B-B
3 B-C
4 B-H
5 C-D
6 D-E
7 E-F
8 G-I
9 I-J
10 I-K
11 K-L
12 K-M
13 M-R
14 P-Q
15 R-S
16 S-T
17 T-U
18 T-V
19 V-W
20 W-X
21 X-Y
22 Y-Z

Angle Coeffs
#
1 Al-G-I
2 B-B-B
3 B-B-C
4 B-B-H
5 B-C-D
6 C-D-E
7 D-E-F
8 F-E-F
9 G-I-J
10 G-I-K
11 I-K-L
12 I-K-M
13 J-I-J
14 J-I-K
15 K-M-R
16 L-K-M

17 M-R-S
18 Q-P-Q
19 R-S-T
20 S-T-U
21 S-T-V
22 T-V-W
23 U-T-U
24 U-T-V
25 V-W-X
26 W-X-Y
27 X-Y-Z
28 Z-Y-Z

Dihedral Coeffs
#
1 Al-G-I-J
2 Al-G-I-K
3 B-B-B-B
4 B-B-B-C
5 B-B-B-H
6 B-B-C-D
7 B-C-D-E
8 C-D-E-F
9 G-I-K-L
10 G-I-K-M
11 I-K-M-R
12 J-I-K-L
13 J-I-K-M
14 K-M-R-S
15 L-K-M-R
16 M-R-S-T
17 R-S-T-U
18 R-S-T-V
19 S-T-V-W
20 T-V-W-X
21 U-T-V-W
22 V-W-X-Y
23 W-X-Y-Z

Improper Coeffs
#
1 X-Z-Y-Z

Force field definition

```
pair_style hybrid lj/cut/coul/long 14.0 12.0 lj/cut/coul/long 14.0 12.0 &
        lj/cut/coul/long 14.0 12.0

kspace_style pppm 1.0e-5

special_bonds lj 0.0 0.0 0.000000000000000001 coul 0.0 0.0 0.000000000000000001

pair_modify mix arithmetic

pair_coeff   1   1 lj/cut/coul/long 1    0.0000013298  4.2712 #Al
pair_coeff   2   2 lj/cut/coul/long 1    0.0914113617  3.9500 #B
pair_coeff   3   3 lj/cut/coul/long 1    0.0914113617  3.9500 #C
pair_coeff   4   4 lj/cut/coul/long 1    0.1700000000  3.0000 #D
pair_coeff   5   5 lj/cut/coul/long 1    0.2500000000  3.4000 #E
pair_coeff   6   6 lj/cut/coul/long 1    0.2000000000  3.1500 #F
pair_coeff   7   7 lj/cut/coul/long 1    0.1700000000  3.0000 #G
pair_coeff   8   8 lj/cut/coul/long 1    0.1947459446  3.7500 #H
pair_coeff   9  9 lj/cut/coul/long  1    0.0500000000  3.8000 #I
pair_coeff   10 10 lj/cut/coul/long 1    0.2070000000  3.7750 #J
pair_coeff   11 11 lj/cut/coul/long 1    0.1050000000  3.7500 #K
pair_coeff   12 12 lj/cut/coul/long 1    0.2100000000  2.9600 #L
pair_coeff   13 13 lj/cut/coul/long 1    0.1700000000  3.0000 #M
pair_coeff   14 14 lj/cut/coul/long 1    0.3500000000  2.1600 #N
pair_coeff   15 15 lj/cut/coul/long 1    0.1554300000  3.1655 #O
pair_coeff   16 16 lj/cut/coul/long 1    0.1553625123  3.1660 #P
pair_coeff   17 17 lj/cut/coul/long 1    0.0000000000  0.0000 #Q
pair_coeff   18 18 lj/cut/coul/long 1    0.1180000000  3.9050 #R
pair_coeff   19 19 lj/cut/coul/long 1    0.1450000000  3.9600 #S
pair_coeff   20 20 lj/cut/coul/long 1    0.1700000000  3.2500 #T
pair_coeff   21 21 lj/cut/coul/long 1    0.1450000000  3.9600 #U
pair_coeff   22 22 lj/cut/coul/long 1    0.1450000000  3.9600 #V
pair_coeff   23 23 lj/cut/coul/long 1    0.1180000000  3.9050 #W
pair_coeff   24 24 lj/cut/coul/long 1    0.1180000000  3.9050 #X
pair_coeff   25 25 lj/cut/coul/long 1    0.1050000000  3.7500 #Y
pair_coeff   26 26 lj/cut/coul/long 1    0.2100000000  2.9600 #Z

pair_coeff   2  4 lj/cut/coul/long 2 0.15068361  3.74939995
pair_coeff   2  5 lj/cut/coul/long 2 0.13514586  3.5273928
pair_coeff   3  6 lj/cut/coul/long 2 0.13514586  3.5273928

pair_coeff   1  10 lj/cut/coul/long 3 0.0005246605    4.0231
pair_coeff   1  11 lj/cut/coul/long 3 0.0003736696    4.0106
pair_coeff   7  12 lj/cut/coul/long 3 0.1889444363    2.9800
pair_coeff   7  13 lj/cut/coul/long 3 0.1700000000    3.0000
```

```
pair_coeff   10 12 lj/cut/coul/long 3 0.2084946042  3.3675
pair_coeff   10 13 lj/cut/coul/long 3 0.1875899784  3.3875
pair_coeff   9  18 lj/cut/coul/long 3 0.0768114575   3.8525
pair_coeff   12 18 lj/cut/coul/long 3 0.1574166446  3.4325
pair_coeff   11 19 lj/cut/coul/long 3 0.1233896268  3.8550
pair_coeff   13 20 lj/cut/coul/long 3 0.1700000000  3.1250
pair_coeff   18 21 lj/cut/coul/long 3 0.1308051987  3.9325
pair_coeff   18 22 lj/cut/coul/long 3 0.1308051987  3.9325
pair_coeff   19 23 lj/cut/coul/long 3 0.1308051987  3.9325
pair_coeff   21 23 lj/cut/coul/long 3 0.1308051987  3.9325
pair_coeff   20 24 lj/cut/coul/long 3 0.1416333294  3.5775
pair_coeff   22 25 lj/cut/coul/long 3 0.1233896268  3.8550
pair_coeff   23 26 lj/cut/coul/long 3 0.1574166446  3.4325

pair_modify pair lj/cut/coul/long 2 special lj 0.0 0.0 0.500
pair_modify pair lj/cut/coul/long 2 special coul 0.0 0.0 0.83333333

pair_modify pair lj/cut/coul/long 3 special lj 0.0 0.0 0.125
pair_modify pair lj/cut/coul/long 3 special coul 0.0 0.0 0.500

bond_style harmonic

bond_coeff  1    320.00        1.425 #Al-G
bond_coeff  2    310.00        1.530 #B-B
bond_coeff  3    310.00        1.530 #B-C
bond_coeff  4    310.00        1.530 #B-H
bond_coeff  5    300.00        1.420 #C-D
bond_coeff  6    300.00        1.580 #D-E
bond_coeff  7    450.00        1.460 #E-F
bond_coeff  8    320.00        1.425 #G-I
bond_coeff  9    260.00        1.526 #I-J
bond_coeff  10   317.00         1.522 #I-K
bond_coeff  11   656.00         1.250 #K-L
bond_coeff  12   320.00         1.425 #K-M
bond_coeff  13   320.00         1.425 #M-R
bond_coeff  14   100.00         1.000 #P-Q
bond_coeff  15   260.00         1.526 #R-S
bond_coeff  16   337.00         1.449 #S-T
bond_coeff  17   337.00         1.449 #T-U
bond_coeff  18   337.00         1.449 #T-V
bond_coeff  19   260.00         1.526 #V-W
bond_coeff  20   260.00         1.526 #W-X
bond_coeff  21   317.00         1.522 #X-Y
bond_coeff  22   656.00         1.250 #Y-Z
```

angle_style harmonic

angle_coeff 1 100.000 111.80 #Al-G-I
angle_coeff 2 62.100 114.00 #B-B-B
angle_coeff 3 62.100 114.00 #B-B-C
angle_coeff 4 62.100 114.00 #B-B-H
angle_coeff 5 62.100 109.50 #B-C-D
angle_coeff 6 62.100 112.60 #C-D-E
angle_coeff 7 51.000 102.60 #D-E-F
angle_coeff 8 51.000 115.40 #F-E-F
angle_coeff 9 80.000 109.50 #G-I-J
angle_coeff 10 80.000 109.50 #G-I-K
angle_coeff 11 70.000 117.00 #I-K-L
angle_coeff 12 80.000 120.40 #I-K-M
angle_coeff 13 63.000 112.40 #J-I-J
angle_coeff 14 63.000 111.10 #J-I-K
angle_coeff 15 100.000 111.80 #K-M-R
angle_coeff 16 80.000 126.00 #L-K-M
angle_coeff 17 80.000 109.50 #M-R-S
angle_coeff 18 300.000 109.47 #Q-P-Q
angle_coeff 19 80.000 111.20 #R-S-T
angle_coeff 20 50.000 121.90 #S-T-U
angle_coeff 21 50.000 121.90 #S-T-V
angle_coeff 22 80.000 111.20 #T-V-W
angle_coeff 23 50.000 121.90 #U-T-U
angle_coeff 24 50.000 121.90 #U-T-V
angle_coeff 25 63.000 112.40 #V-W-X
angle_coeff 26 63.000 112.40 #W-X-Y
angle_coeff 27 70.000 117.00 #X-Y-Z
angle_coeff 28 80.000 126.00 #Z-Y-Z

dihedral_style fourier

dihedral_coeff 1 2 0.100 2 0.0 0.725 3 0.0 #Al-G-I-J
dihedral_coeff 2 2 0.100 2 0.0 0.725 3 0.0 #Al-G-I-K
dihedral_coeff 3 3 0.70551686 1 0.0 -0.135507408 2 180.0 1.57251388 3 0.0 #B-B-B-B
dihedral_coeff 4 3 0.70551686 1 0.0 -0.135507408 2 180.0 1.57251388 3 0.0 #B-B-B-C
dihedral_coeff 5 3 0.70551686 1 0.0 -0.135507408 2 180.0 1.57251388 3 0.0 #B-B-B-H
dihedral_coeff 6 1 1.000 3 0.0 #B-B-C-D
dihedral_coeff 7 1 0.725 3 0.0 #B-C-D-E
dihedral_coeff 8 1 0.250 3 0.0 #C-D-E-F
dihedral_coeff 9 1 0.067 3 180.0 #G-I-K-L

```
dihedral_coeff 10 1 0.067 3 180.0 #G-I-K-M
dihedral_coeff 11 1 0.067 3 180.0 #I-K-M-R
dihedral_coeff 12 1 0.067 3 180.0 #J-I-K-L
dihedral_coeff 13 1 0.067 3 180.0 #J-I-K-M
dihedral_coeff 14 2 0.100 2 0.0 0.725 3 0.0 #K-M-R-S
dihedral_coeff 15 1 0.067 3 180.0 #L-K-M-R
dihedral_coeff 16 1 2.000 3 0.0 #M-R-S-T
dihedral_coeff 17 1 2.500 2 180.0 #R-S-T-U
dihedral_coeff 18 1 2.000 3 0.0 #R-S-T-V
dihedral_coeff 19 1 2.000 3 0.0 #S-T-V-W
dihedral_coeff 20 1 2.000 3 0.0 #T-V-W-X
dihedral_coeff 21 1 2.500 2 180.0 #U-T-V-W
dihedral_coeff 22 1 1.000 3 0.0 #V-W-X-Y
dihedral_coeff 23 1 0.067 3 180.0  #W-X-Y-Z

improper_style cvff

improper_coeff 1 10.5 -1 2 #X-Z-Y-Z

# Define atomic groups
#
group sulfur type 5
group sds type 2 3 4 5 6 8
group na type 14
group al2o3 type 1 15
group water type 16 17
group cbma type 7 9 10 11 12 13 18 19 20 21 22 23 24 25 26
group notal2o3 type 2 3 4 5 6 7 8 9 10 11 12 13 14 16 17 18 19 20 21 22 23 24 25 26

#
velocity sds create 298.0 293288 dist gaussian mom yes rot yes
velocity na create 298.0 293288 dist  gaussian mom yes rot yes
velocity water create 298.0 293288 dist gaussian mom yes rot yes
velocity cbma create 298.0 293288 dist gaussian mom yes rot yes

#
neighbor 2.0 bin
neigh_modify  delay 10 every 1 check yes
neigh_modify exclude group al2o3 al2o3


# VMD V1.9 with Velocity
dump 1 all custom 100 SDS-H2O-CBMA-Al2O3.traj id type x y z xu yu zu vx vy vz fx fy fz
dump_modify 1 sort id
```

```
# XYZ
dump 2 all xyz 5000 structure.*.xyz
dump_modify 2 sort id

compute liquidtemp notal2o3 temp
thermo_modify temp liquidtemp
compute_modify liquidtemp dynamic yes

# RUN @ NVT 298.0 K for 30 ns
fix 1 water shake 0.0001 20 0 b 14 a 18
fix 2 notal2o3  nvt temp 298.0 298.0 100.0
fix 3 al2o3 setforce 0.0 0.0 0.0

thermo 100
thermo_style custom step vol temp press pe ke etotal enthalpy evdwl ecoul elong &
        etail lx ly lz epair ebond eangle edihed eimp emol pxx pyy pzz pxy pxz pyz &
        fmax c_liquidtemp
thermo_modify line one

run 30000000
```

Appendix B: CBMA Legend and Charges

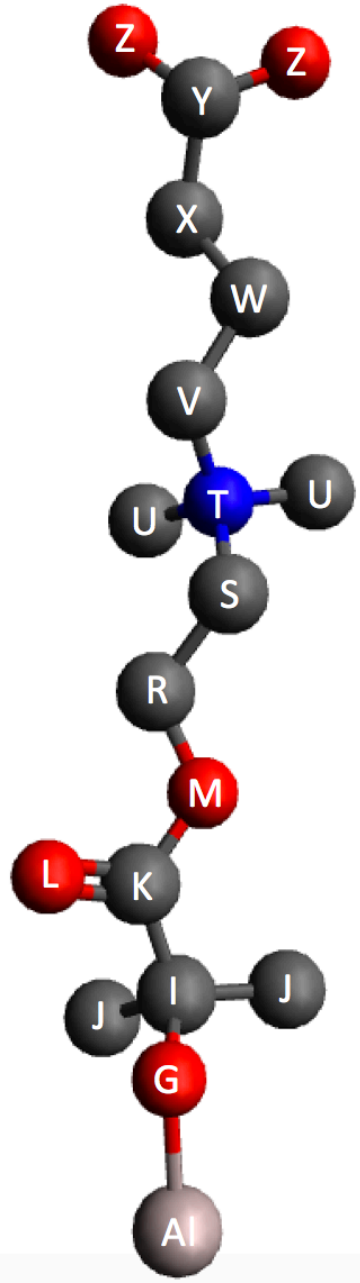

Atom Type	Charge (e)
G	-0.4000
I	+0.2900
J	+0.0600
K	+0.5500
L	-0.4500
M	-0.4000
R	+0.2900
S	+0.2500
T	0.0000
U	+0.2500
V	+0.2500
W	0.0000
X	-0.1000
Y	+0.7000
Z	-0.8000